3-D Laminar Stationary Flow over a Porous Surface with Suction: Description at Pore Level

Philippe Schmitz and Marc Prat
Institut de Mécanique des Fluides, URA-CNRS D0005, 31400 Toulouse, France

The microhydrodynamics associated with membrane cross-flow microfiltration processes is analyzed. To this end, numerical computations of the flow near a pore of a spatially periodic model porous surface are performed for various porosities and suction conditions. The structure of the fluid capture tube as well as related fluid dynamics aspects, such as the existence of a recirculating eddy in the pore, the slip velocity at the wall, and the pressure drop across the pore, are investigated. In particular, the influence of the neighbor pores on the structure of the fluid capture tube of a given pore is studied.

Introduction

The problem of particle entrapment from a suspension shear flow past a porous surface with suction has a fundamental application in cross-flow microfiltration in order to understand the limiting phenomenon of membrane fouling. Indeed it is commonly admitted that particle deposition and aggregation at the membrane surface is the first and one of the major factors in the fouling mechanism. The motion of small particles of several microns range is directly connected to fluid flow if we neglect gravity effects. The first necessary step consists in analyzing and modeling hydrodynamics in the near-field region of a porous surface with suction and especially close to a pore of this porous surface.

Recent works have been published on the problem of shear flow over a small circular side pore. The main application was blood flow and, more precisely, microcirculatory behavior involving the distribution of the cellular components of blood. Tutty (1988) modeled the problem of linear shear flow along a flat wall, past an infinitely deep circular hole perpendicular to the wall, with fluid being sucked into the hole. By assuming Stokes flow, the three-dimensional problem was reduced to two independent problems on a two-dimensional domain. Regions of high and low wall shear stress have been located to determine where atherosclerotic lesions occur in blood vessels. An analogous problem has been considered by Yan et al. (1991) and Wu et al. (1992) in order to better understand the phenomenon of defect of discharge hematocrit into the side branch compared to the feed reservoir hematocrit and its variation with the shear flow rate. Two underlying mechanisms were considered: the fluid skimming from the particle-free layer at the main tube wall (Yan et al., 1991) and the particle screening due to the hydrodynamic interaction with the pore entrance (Wu et al., 1992). These studies were also at low Reynolds number and applied a simplified description of flow as a linear combination of a Sampson flow, that is, the flow through a circular hole in a plane, and a simple shear flow according to Dagan et al. (1982). This assumption implied that the authors neglected the counterrotating vortex flow within the side branch, obtained by Tutty (1988) in some cases, since transverse velocity at the mouth of the pore was taken equal to zero. However, they showed that this simplified solution could accurately represent the flow within the upper half-space over the pore, except for the location of the wall attachment point. The results were found to be qualitatively similar to the experimental observations of the hematocrit defect in microcirculation.

In the context of cross-flow microfiltration, a two-dimensional approach has been developed by Schmitz et al. (1992) on the problem of shear flow past a porous surface and its subsequent effect on particle deposition at the membrane surface. This numerical study computed Stokes flow near a single pore of the porous surface with suction. The authors have shown the existence of two flow structures, related to the intensity of suction, which determines the possible particle deposition. Results in terms of streamlines were of the same type as the ones obtained by Tutty (1988) in three dimensions. Particularly, they showed the existence of a recirculating vortex flow within the pore at low suction, preventing particle entrapment. But two aspects had still to be examined: the influence of the surface porosity on the flow structure and, more precisely, on the fluid capture tube and its shape, and also the characterization of the three-dimensional effect, since the two-dimensional study modeled the pore as

a slot of infinite lateral extension. The first aspect requires accounting for the existence of numerous pores at the surface, that is, the influence of neighbor pores on the flow near a given pore. None of the previous works considered such an influence because they analyzed a channel flow with a single small side branch or with noninteracting pores. Moreover, we have to consider the exact Stokes solution instead of the approximate Sampson solution, since determining the flow structure within the pore is of great interest for the understanding of particle behavior.

Accordingly this article proposes a three-dimensional approach to fluid flow near a circular pore of a porous surface with suction. This pore is one of the million pores of the porous surface. In fact, the model porous surface is a spatially periodic porous surface. This enables us to make use of periodic boundary conditions in order to compute the fluid flow over a representative unit cell of the porous surface in which a cylindrical pore is supposed to be centered. First, the local problem allowing one to compute the flow in the near wall region is established. The problem is solved by means of a finite element method. Subsequently, we discuss the existence of a slip velocity at the porous wall. Influence of such a slip velocity at a membrane surface on ultrafiltration performance has been studied by Singh and Laurence (1979) from a theoretical standpoint. Effect of the slip velocity on the structure of the flow in the entrance of a porous pipe was reported by Tanahashi et al. (1982). Our simulations show that the slip effect is practically negligible, at least for the porous surface considered in this article. We then study the flow through the membrane and show that the pressure drop across the membrane can be simply estimated by assuming a Poiseuille flow within the pore. The last part of the article is essentially devoted to studying the fluid capture tube, that is, the region occupied by fluid that is eventually sucked down the pore. Related fluid dynamics aspects, such as the existence of a vortex in the pore, are also discussed.

Formulation

Near wall model

We are especially interested in studying the performance of a pressure-driven membrane process such as cross-flow microfiltration. In this technique, the microporous membrane is the inner skin of a highly porous support channel or tube so that the pressure drop through the total porous wall is mainly due to the transmembrane pressure drop. As stated earlier, we study the flow in the vicinity of the membrane, that is, the near wall region. To be more specific, we propose to compute the flow within a small region of the fluid domain containing a representative element of the membrane structure. This implies that we must be able to specify appropriate boundary conditions at the boundaries of the small region of interest. It should be obvious that defining such appropriate boundary conditions, that is, restricting the flow computation to a small region, is not always possible. Thus, our approach relies on a certain number of assumptions that should be clearly stated. To begin with, however, we consider the whole fluid domain. For simplicity, we consider a channel of infinite lateral extension. The upper and lower walls of the channel are porous and have the same porous structure. The fluid is incompressible and Newtonian. There are no external forces.

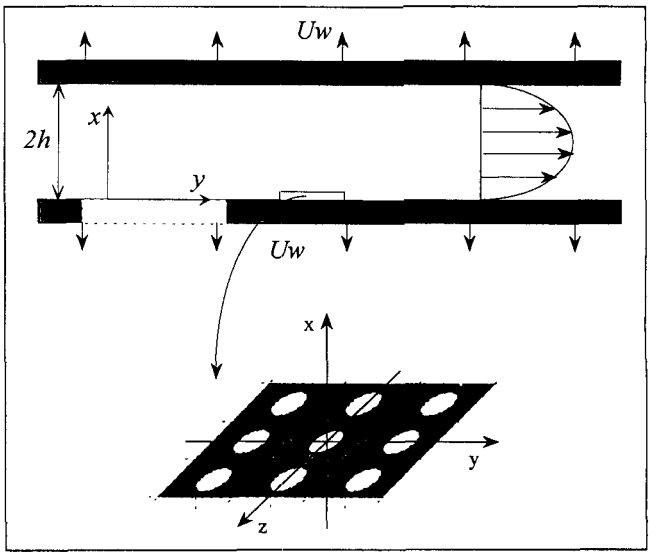

Figure 1. Flow geometry; spatially periodic model porous surface.

The flow is laminar and steady. A coordinate system is chosen with the origin at the porous wall, Figure 1. The direction of the tangential main flow over the surface is the y direction, while the direction of suction through the pores perpendicular to the surface is the x direction. The distance between the walls is taken to be $2h$ and the channel length is L. The walls are assumed to be a spatially periodic porous surface with a square arrangement of pores, as shown in Figure 1. The pores are circular and of monodispersed radius r. Naturally, the idea we have in mind is to study the flow over a unit cell of this surface only. We also suppose that the mean suction velocity through the pore is $u_p = u_w/\epsilon$, where ϵ is the surface porosity. Under the assumed conditions, the flow within the channel is governed by the Navier–Stokes equations,

$$\rho(\boldsymbol{u}\cdot\nabla\boldsymbol{u}) = -\nabla p + \mu\nabla^2\boldsymbol{u}, \tag{1}$$

and the continuity equation,

$$\nabla\cdot\boldsymbol{u} = 0, \tag{2}$$

with $\boldsymbol{u} = (u, v, w)$.

Concerning the boundary conditions, we can assume that we know the velocity and pressure distributions, denoted $\boldsymbol{u}_0$, p_0, at the entrance of the channel. At the center of the channel, symmetry conditions can be imposed, $\partial v/\partial x = 0$, $u = w = 0$ at $x = h$. At the solid part of the porous surface, the nonslip boundary condition is imposed, $\boldsymbol{u} = 0$ at Γ_s. At the fluid part of the porous surface, we ignore the boundary conditions since in fact the fluid domain is not limited to the channel, but includes the pore space within the porous walls and the external fluid region located above and below the porous walls. Clearly, a full and detailed treatment of the problem would require solving the Navier–Stokes equations not only within the channel but also within the pore space and the external fluid regions. Naturally, this is far beyond

the scope of the present article. As far as we are concerned, we simply state that the solution of the problem under consideration should meet the following two conditions:

$$\langle v\rangle^f = \frac{1}{\Gamma_f}\int_{\Gamma_f} v\, dA = v_s; \qquad \langle u\rangle^f = u_p, \tag{3}$$

where v_s is the slip velocity at the wall, Beavers and Joseph (1967). At this stage, we study the solution of the preceding problem in terms of the following decomposition,

$$\boldsymbol{u} = \bar{\boldsymbol{u}} + \tilde{\boldsymbol{u}} \tag{4}$$

$$p = \bar{p} + \tilde{p} \tag{5}$$

where $\bar{\boldsymbol{u}}$ and $\bar{p}$ are given by the following problem,

$$\rho(\bar{\boldsymbol{u}}\cdot\nabla\bar{\boldsymbol{u}}) = -\nabla\bar{p} + \mu\nabla^2\bar{\boldsymbol{u}} \tag{6}$$

$$\nabla\cdot\bar{\boldsymbol{u}} = 0 \tag{7}$$

$$\frac{\partial\bar{v}}{\partial x} = 0, \quad \bar{u} = \bar{w} = 0 \text{ at } x = h. \tag{8}$$

$$\bar{v} = v_s; \qquad \bar{u} = u_w \text{ at } x = 0. \tag{9}$$

$$\bar{\boldsymbol{u}} = \boldsymbol{u}_0; \quad \bar{p} = p_0 \text{ at the entrance of the channel.} \tag{10}$$

This type of problem has been studied by many authors since the pioneer work of Berman (1953). Contrary to the previously considered velocity and pressure fields, that is, $\boldsymbol{u}$ and p, $\bar{\boldsymbol{u}}$ and $\bar{p}$ do not depend on the small spatial scale b associated with the heterogeneous structure of the membrane, Figures 1 and 2. In some sense, $\bar{\boldsymbol{u}}$ and $\bar{p}$ represent spatially averaged velocity and pressure. Let us now consider the perturbation fields $\tilde{\boldsymbol{u}}$ and $\tilde{p}$. The governing equations for these fields are obtained by substituting Eqs. 4 and 5 into Eqs. 1 and 2. Taking into account Eqs. 6–10 and the associated boundary conditions, this leads to,

$$\rho(\tilde{\boldsymbol{u}}\cdot\nabla\tilde{\boldsymbol{u}}) = -\nabla\tilde{p} + \mu\nabla^2\tilde{\boldsymbol{u}} - \underline{\rho(\bar{\boldsymbol{u}}\cdot\nabla\tilde{\boldsymbol{u}})} - \underline{\rho(\tilde{\boldsymbol{u}}\cdot\nabla\bar{\boldsymbol{u}})} \tag{11}$$

$$\nabla\cdot\tilde{\boldsymbol{u}} = 0 \tag{12}$$

$$\frac{\partial\tilde{v}}{\partial x} = 0, \qquad \tilde{u} = \tilde{w} = 0 \text{ at } x = h. \tag{13}$$

$$\tilde{v} = v - v_s; \qquad \tilde{u} = u - u_w; \qquad \tilde{w} = w \text{ at } x = 0. \tag{14}$$

$$\tilde{\boldsymbol{u}} = 0; \qquad \tilde{p} = 0 \text{ at the entrance of the channel.} \tag{15}$$

We also have

$$\langle\tilde{\boldsymbol{u}}\rangle = \frac{1}{\Gamma}\int_{\Gamma}\tilde{\boldsymbol{u}}\, dA = 0 \qquad \text{at } x = 0 \text{ where } \Gamma = \Gamma_f \cup \Gamma_s. \tag{16}$$

From these equations, it can be seen that the perturbation fields, $\tilde{\boldsymbol{u}}$ and $\tilde{p}$, depend on the boundary conditions at the porous wall, Eq. 14, and the volume source terms associated with inertia effects, which are underlined in Eq. 11. At this stage, because of the volume source terms, it can be seen that the perturbation fields do not generally vanish outside some near wall region. Accordingly, without any further assumption, it is not correct to study the channel flow problem in terms of the "averaged" fields $\bar{\boldsymbol{u}}$ and $\bar{p}$, as defined by Eqs. 6–10, for the flow does not reduce to a two-dimensional flow. It may "feel" the heterogeneous nature of the wall up to the center of the channel. This case corresponds to relatively high Reynolds number flows in channels of small width, that is, such that the channel width is not much greater than the size of the pore. Fortunately, this is not the situation typically encountered in practice. Generally, the channel width is much greater than the pore size, that is, $r = \lambda h$ with $\lambda \ll 1$ where r is the mean radius of the membrane pore. Under these circumstances, the inertial effects are negligible in the near wall region. More precisely, the Reynolds numbers generally defined for characterizing the flow in the system are the channel Reynolds number, $Re = (2v_D h/\nu)$, where v_D is the velocity averaged over the channel cross section, and the filtration Reynolds number, $Re_w = (u_w h/\nu)$. Taking b as length scale of the near wall region, we may define two Reynolds numbers for characterizing the flow within the near wall region, $Re_t = (v_b b/\nu)$ where v_b is on the order of the Poiseuille velocity at the distance b from the wall and $Re_n = (u_w b/\nu)$. Clearly, Re_t and Re_n characterize the tangential flow and the flow normal to the wall, respectively. It is straightforward to obtain

$$Re_t \approx O(\lambda^2 Re) \qquad \text{and} \qquad Re_n \approx O(\lambda Re_w). \tag{17}$$

As λ is typically of the order of 10^{-3} and as Re_w is typically in the range $0 < Re_w < 30$, it can be concluded that the inertial effects are negligible in the near wall region. Consequently, we make the reasonable assumption that $Re_t \ll 1$ and $R_n \ll 1$. Therefore, the underlined terms in Eq. 11 can be neglected. The perturbation fields are then only controlled by the boundary conditions at the wall. As moreover $\langle\tilde{\boldsymbol{u}}\rangle = 0$, it is clear that the perturbation fields are not zero only in the region close to the wall, the thickness of which is of the order of b. Finally, the flow in the system can be analyzed in terms of an inner core region where the flow is two-dimensional and can be computed by solving Eqs. 6–10, and of a near wall region where the flow is three-dimensional and "feels" the small-scale variations associated with the discrete distribution of the pores. We are now in a much better position to compute the near wall flow since we know the boundary condition to be imposed at some distance δ of the wall where the perturbation fields vanish, that is, $\boldsymbol{u} = \bar{\boldsymbol{u}}$ at $x = \delta$. We are left with the remaining boundary conditions. In fact, since our model membrane is spatially periodic, we want to compute the near wall flow over a unit cell of the membrane only, that is, over the control volume sketched in Figure 2. To this end, we would like to make use of periodic boundary conditions in the y and z directions. *A priori*, the flow need not, however, be periodic in the y direction since part of the flow is sucked down the pore. A little thought indicates that the flow sucked down the pore comes on the one part from the inner core region and on the other part from the near wall region located upstream. At this point, we need to evaluate the flux of mass leaving and entering through the surfaces limiting the control volume. In fact, we want to derive conditions under which all the fluid sucked down the pore may be seen as coming from the inner core region. To this end, let us go

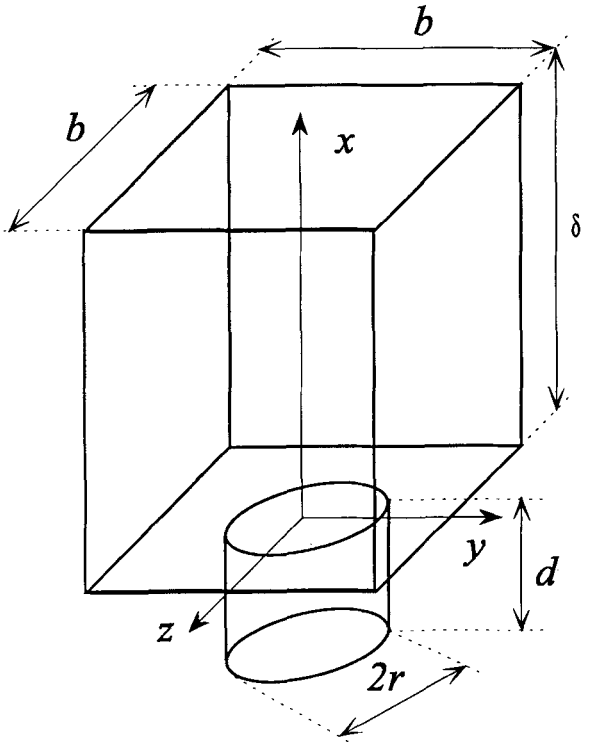

Figure 2. Computational domain.

back to the inner core problem, Eqs. 6–10. This problem has been studied in particular by Berman (1953), Terril (1964), Terril and Thomas (1969) in terms of similarity solutions. More recently, Durlofsky and Brady (1984) have studied the validity of these solutions and have shown that under certain circumstances a similarity solution cannot be found for the axisymmetric flows, while similarity solutions to the channel case exist for all values of the Reynolds number. Assuming a uniform suction or injection, Brady (1984) has also shown that the flow within the channel is determined by the inlet condition when the filtration Reynolds number Re_w is above a critical value, 2.3, for the axisymmetric case and 6 for the channel case. On the other hand, it may also be concluded from the study of Brady that the similarity solution is accurate for $Re_w \leq 1$. Furthermore, in this case, we may use the solution derived by Berman (1953), which is valid for small Re_w. Berman's solution has been derived under the assumption of uniform filtration velocity at the wall. In many real systems, this assumption is not valid. However, since the typical size b of a cell of the membrane is much smaller than the length L of the channel, it is reasonable to admit that the filtration velocity at the wall is locally uniform and therefore to make use of Berman's solution locally. Also, Berman has neglected the slip effect at the wall. This is not, however, a severe restriction since, as we shall see, the slip effect is indeed very weak. According to Berman, the velocities at $x = \delta$ are given by

$$\bar{v}(y,\delta) = \frac{3}{2}\left[v_D - \frac{u_w y}{h}\right](1-\eta^2)\left(1 - \frac{Re_w}{420}(2-7\eta^2-7\eta^4)\right) \tag{18}$$

$$\bar{u}(\delta) = 0.5u_w\eta(3-\eta^2) - \frac{Re_w}{280}\eta(2-3\eta^2+\eta^6), \tag{19}$$

where $\eta = 1-(\delta/h)$ and v_D is the velocity averaged over the channel cross section at $y = 0$, that is, $v_D = (1/2h)\int_0^{2h} \bar{v}(x, 0)\,dx$.

As $(\delta/h) \ll 1$, we deduce from Eqs. 18 and 19,

$$\bar{v}(y,\delta) \approx 3\left[v_D - \frac{u_w y}{h}\right]\frac{\delta}{h}\left(1+\frac{Re_w}{35}\right) \approx 3\left[v_D - \frac{u_w y}{h}\right]\frac{\delta}{h} \tag{20}$$

$$\bar{u}(\delta) \approx u_w\left(1-\left(\frac{\delta}{h}\right)^2\right) \approx u_w. \tag{21}$$

Similarly, for $(\delta/h) \ll 1$, Berman solution yields the following expression for the pressure field,

$$\bar{p}(y,\delta) \approx \frac{\left(-3+\frac{81}{35}Re_w\right)\mu}{h^2}\left[v_D y - \frac{u_w y^2}{2h}\right] - \rho\frac{u_w^2}{2}\left(1-2\left(\frac{\delta}{h}\right)^2\right) + \frac{u_w\mu}{h}\left(2-2\frac{\delta}{h}\right) + \text{const.} \tag{22}$$

From Eq. 21, it can be seen that, in terms of mass balance over the domain of interest, the flux of mass leaving the control volume through the pore is equal to the flux of mass entering the control volume through the top side of the control volume. Taking into account the spatially periodic structure of the model membrane, this implies that the velocity fields are locally spatially periodic in the y and z directions. Therefore, it can be concluded that we can make use here of the periodic boundary condition in the y and z directions. Finally, we are only left with the boundary condition to be imposed at the exit of the pore. As the entrance length is very short at low Reynolds number, a Poiseuille velocity profile is imposed at the exit of the pore. This condition is discussed in more details in the section titled "Fluid flow near a pore with suction."

Finally, in a coordinate system with the origin at the center of a spatial period, such as the one sketched in Figure 2, the problem to be solved takes the following form:

$$\nabla\cdot\boldsymbol{u} = 0 \tag{23}$$

$$\mu\nabla^2\boldsymbol{u} - \nabla p = 0. \tag{24}$$

Upper fluid boundary.

$$\boldsymbol{u} = (-u_w, \bar{v} + v_s, 0) \qquad \text{at } x = \delta. \tag{25}$$

Pore exit boundary.

$$\boldsymbol{u} = \left(2u_p\left(1-\frac{y^2+z^2}{r^2}\right),0,0\right) \qquad \text{at } x = -d, \quad y^2+z^2 \leq r^2. \tag{26}$$

Periodic boundary.

$$\boldsymbol{u}(y = -b/2) = \boldsymbol{u}(y = b/2) \tag{27}$$

$$u(z=-b/2)=u(z=b/2) \tag{28}$$

$$p(y=-b/2)=p(y=b/2)+bF_y \tag{29}$$

$$p(z=-b/2)=p(z=b/2). \tag{30}$$

Solid boundary.

$$u=0 \qquad \text{at } x=0, \qquad y^2+z^2\geq r^2 \tag{31}$$

$$u=0 \qquad \text{at } -d\leq x\leq 0, \qquad y^2+z^2=r^2 \tag{32}$$

where here $u_w=(\pi r^2/b^2)u_p$. In Eq. 25, v_s is the slip velocity seen at the macroscopic level, Beavers and Joseph (1967). The specific study of this boundary condition is detailed in the section titled "Slip coefficient." In Eq. 29, F_y is the macroscopic mean pressure gradient in the channel, that is, $\partial\bar{p}/\partial y$. Indeed, it follows from Eq. 5, that

$$p(y=-b/2)-p(y=b/2)=\bar{p}(y=-b/2)-\bar{p}(y=b/2)+\tilde{p}(y=-b/2)-\tilde{p}(y=b/2). \tag{33}$$

As $\tilde{p}$ is spatially periodic in the y direction, Eq. 33 leads to

$$p(y=-b/2)-p(y=b/2)=\bar{p}(y=-b/2)-\bar{p}(y=b/2). \tag{34}$$

Making use of the Berman solution for the pressure distribution, Eq. 22, one obtains

$$p(y=-b/2)-p(y=b/2)=b\frac{\partial\bar{p}}{\partial y}=-\frac{b\mu}{h^2}\left(-3+\frac{81}{35}Re_w\right)v_D=bF_y. \tag{35}$$

As F_y is not zero, Eq. 29 is not a periodic boundary condition. In order to transform this boundary condition into a periodic one, we express the local problem in terms of u and $\tilde{p}$. To this end, we substitute the pressure decomposition, Eq. 5, into Eqs. 23–32 to obtain

$$\nabla\cdot\boldsymbol{u}=0 \tag{36}$$

$$\mu\nabla^2\boldsymbol{u}-\nabla\tilde{p}=\boldsymbol{j}F_y \tag{37}$$

$$\boldsymbol{u}=(-u_w,\bar{v}+v_s,0) \qquad \text{at } x=\delta \tag{38}$$

$$\boldsymbol{u}=\left(2u_p\left(1-\frac{y^2+z^2}{r^2}\right),0,0\right) \qquad \text{at } x=-d, y^2+z^2\leq r^2 \tag{39}$$

$$\boldsymbol{u}(y=-b/2)=\boldsymbol{u}(y=b/2) \tag{40}$$

$$\boldsymbol{u}(z=-b/2)=\boldsymbol{u}(z=b/2) \tag{41}$$

$$\tilde{p}(y=-b/2)=\tilde{p}(y=b/2) \tag{42}$$

$$\tilde{p}(z=-b/2)=\tilde{p}(z=b/2). \tag{43}$$

$$u=0 \qquad \text{at } x=0, \qquad y^2+z^2\geq r^2 \tag{44}$$

$$u=0 \qquad \text{at } -d\leq x\leq 0, \qquad y^2+z^2=r^2 \tag{45}$$

where $\boldsymbol{j}$ denotes the unit vector in the y direction. Note that the macroscopic mean pressure gradient F_y appears as a given body force in Eq. 37. In Eq. 37, we have only kept the y component of $\nabla\bar{p}$. Indeed, making use of Berman solution, Eq. 22 leads to

$$\frac{\dfrac{\partial\bar{p}}{\partial y}}{\dfrac{\partial\bar{p}}{\partial x}}=0.5\frac{Re}{Re_w}\left(-3+\frac{81}{35}Re_w\right) \qquad \delta/h\ll 1 \tag{46}$$

which shows that $\partial\bar{p}/\partial x$ can be neglected, since $Re\gg Re_w$ and $Re_w\leq 1$.

Finally, this problem accounts for the flow in the near wall region under the following assumptions:

- Spatially periodic membrane
- Steady laminar flow in the channel
- $b/h\ll 1$; $b/L\ll 1$
- Inertia negligible within the near wall region
- $Re_w\leq 1$

To derive this local problem, we have considered a channel with parallel porous walls. However, this problem is also representative of the local microhydrodynamics in a tube, provided the tube radius is large compared to the size b of the unit cell of the membrane.

Superposition principle

For convenience the problem is expressed in dimensionless form adopting r and $\bar{v}_\delta=\bar{v}$ at $x=\delta$ as length scale and velocity scale, respectively (note that, under the assumptions listed earlier, the variation of $\bar{v}_\delta$ as a function of y can be neglected over a distance on the order of b). In terms of the dimensionless variables $x^*=x/r$, $u^*=u/\bar{v}_\delta$, and $p^*=(rp/\mu\bar{v}_\delta)$, the local problem in which the * has been omitted for the variables, becomes

$$\nabla\cdot\boldsymbol{u}=0 \tag{47}$$

$$\nabla^2\boldsymbol{u}-\nabla\tilde{p}=\boldsymbol{j}F_y^* \tag{48}$$

$$\boldsymbol{u}=\left(-\frac{\pi}{b^{*2}}\gamma_v,1+\frac{2}{\alpha\delta^*},0\right) \qquad \text{at } x=\delta^* \tag{49}$$

$$\boldsymbol{u}=(2\gamma_v(1-y^2-z^2),0,0) \qquad \text{at } x=-d^*, \qquad y^2+z^2\leq 1 \tag{50}$$

$$\boldsymbol{u}(y=-b^*/2)=\boldsymbol{u}(y=b^*/2) \tag{51}$$

$$\boldsymbol{u}(z=-b^*/2)=\boldsymbol{u}(z=b^*/2) \tag{52}$$

$$\tilde{p}(y=-b^*/2)=\tilde{p}(y=b^*/2) \tag{53}$$

$$\tilde{p}(z=-b^*/2)=\tilde{p}(z=b^*/2) \tag{54}$$

$$u=0 \qquad \text{at } x=0, \qquad y^2+z^2\geq 1 \tag{55}$$

$$u=0 \qquad \text{at } -d^*\leq x\leq 0, \qquad y^2+z^2=1 \tag{56}$$

where $\delta^*=\delta/r$, $h^*=h/r$, $b^*=b/r$, $d^*=d/r$, $F_y^*=(r^2/\mu\bar{v}_\delta)F_y$. The parameter $\gamma_v=u_p/\bar{v}_\delta$ is a velocity ratio that defines the relative suction magnitude. To derive Eq. 49, a

slip boundary condition similar to the Beavers and Joseph (1967) boundary condition is used. In this equation, α is the slip coefficient. The slip boundary condition is discussed in detail in the section titled "Slip coefficient."

Finally, because of the linearity of the Stokes equations, the general problem described by Eqs. 47–56 can be split into three independent problems. Problem 1 corresponds to a Couette flow past a cylindrical cavity, Problem 2 corresponds to the pressure-driven flow past a cylindrical cavity, while Problem 3 corresponds to the uniform flow through a circular constriction.

Problem 1.

$$\nabla\cdot\boldsymbol{u}=0 \tag{57}$$

$$\nabla^2\boldsymbol{u}-\nabla\tilde{p}=0 \tag{58}$$

$$\boldsymbol{u}=\left(0{,}1+\frac{2}{\alpha\delta^*},0\right) \qquad \text{at } x=\delta^* \tag{59}$$

$$\boldsymbol{u}=(0,0,0) \qquad \text{at } x=-d^*, \qquad y^2+z^2\le 1 \tag{60}$$

$$\boldsymbol{u}(y=-b^*/2)=\boldsymbol{u}(y=b^*/2) \tag{61}$$

$$\boldsymbol{u}(z=-b^*/2)=\boldsymbol{u}(z=b^*/2) \tag{62}$$

$$\tilde{p}(y=-b^*/2)=\tilde{p}(y=b^*/2) \tag{63}$$

$$\tilde{p}(z=-b^*/2)=\tilde{p}(z=b^*/2) \tag{64}$$

$$\boldsymbol{u}=0 \qquad \text{at } x=0, \qquad y^2+z^2\ge 1 \tag{65}$$

$$\boldsymbol{u}=0 \qquad \text{at } -d^*\le x\le 0, \qquad y^2+z^2=1 \tag{66}$$

Problem 2.

$$\nabla\cdot\boldsymbol{u}=0 \tag{67}$$

$$\nabla^2\boldsymbol{u}-\nabla\tilde{p}=jF_y^* \tag{68}$$

$$\boldsymbol{u}=(0,0,0) \qquad \text{at } x=\delta^* \tag{69}$$

$$\boldsymbol{u}=(0,0,0) \qquad \text{at } x=-d^*, \qquad y^2+z^2\le 1 \tag{70}$$

$$\boldsymbol{u}(y=-b^*/2)=\boldsymbol{u}(y=b^*/2) \tag{71}$$

$$\boldsymbol{u}(z=-b^*/2)=\boldsymbol{u}(z=b^*/2) \tag{72}$$

$$\tilde{p}(y=-b^*/2)=\tilde{p}(y=b^*/2) \tag{73}$$

$$\tilde{p}(z=-b^*/2)=\tilde{p}(z=b^*/2) \tag{74}$$

$$\boldsymbol{u}=0 \qquad \text{at } x=0, \qquad y^2+z^2\ge 1 \tag{75}$$

$$\boldsymbol{u}=0 \qquad \text{at } -d^*\le x\le 0, \qquad y^2+z^2=1 \tag{76}$$

Problem 3.

$$\nabla\cdot\boldsymbol{u}=0 \tag{77}$$

$$\nabla^2\boldsymbol{u}-\nabla\tilde{p}=0 \tag{78}$$

$$\boldsymbol{u}=\left(-\frac{\pi}{b^{*2}}\gamma_v,0,0\right) \qquad \text{at } x=\delta^* \tag{79}$$

$$\boldsymbol{u}=(2\gamma_v(1-y^2-z^2),0,0) \qquad \text{at } x=-d^*, \qquad y^2+z^2\le 1 \tag{80}$$

$$\boldsymbol{u}(y=-b^*/2)=\boldsymbol{u}(y=b^*/2) \tag{81}$$

$$\boldsymbol{u}(z=-b^*/2)=\boldsymbol{u}(z=b^*/2) \tag{82}$$

$$\tilde{p}(y=-b^*/2)=\tilde{p}(y=b^*/2) \tag{83}$$

$$\tilde{p}(z=-b^*/2)=\tilde{p}(z=b^*/2) \tag{84}$$

$$\boldsymbol{u}=0 \qquad \text{at } x=0, \qquad y^2+z^2\ge 1 \tag{85}$$

$$\boldsymbol{u}=0 \qquad \text{at } -d^*\le x\le 0, \qquad y^2+z^2=1. \tag{86}$$

The solution of the general problem is then found by superposition of the solutions of Problems 1, 2 and 3. This procedure is used to reduce the number of computations. Indeed, one case, related to a specific geometry characterized by its porosity ϵ, needs no more than one computation for each problem. The solutions for various F_y^* and γ_v are obtained directly by a simple linear combination of the solutions of Problem 1, Problem 2 for a given F_y^{*0}, and Problem 3 for a given γ_v^0,

$$\boldsymbol{u}=\boldsymbol{u}_1+\boldsymbol{u}_2\frac{F_y^*}{F_y^{*0}}+\boldsymbol{u}_3\frac{\gamma_v^*}{\gamma_v^{*0}}, \tag{87}$$

where $\boldsymbol{u}_1$, $\boldsymbol{u}_2$, and $\boldsymbol{u}_3$ are the solutions of Problem 1, 2 and 3, respectively.

Slip coefficient

As shown in the section on the near wall model, the velocity is uniform at a distance δ from the wall provided that δ is large enough compared to r. This velocity is given by the inner core problem, Eqs. 6–10. In the absence of suction or injection, the inner core problem amounts to the classic problem of determining the macroscopic flow in a porous channel. As is well known, the main difficulty of this classic problem is the boundary condition to be imposed at the porous wall, that is, at $x=0$ in our coordinate system. The most classic condition is the slip boundary condition proposed by Beavers and Joseph (1967),

$$\left.\frac{\partial v}{\partial x}\right|_{x=0}=-\frac{\alpha}{\sqrt{K}}(v_s-V), \tag{88}$$

where V is the filtration velocity in the porous wall in the direction of the external flow, K is the permeability of the porous wall assumed to be homogeneous and isotropic, and the parameter α is the dimensionless slip coefficient. For extensive discussion on this condition, see Vignes-Adler et al. (1987), Kaviany (1991), Larson and Higdon (1986, 1987) and references therein. In brief, the Beavers–Joseph slip boundary condition can be used provided that there is no ambiguity regarding the location of the porous wall, Saffman (1971). As there is no such ambiguity in our numerical study, we are simply left with the determination of the slip coefficient α. It can be proved that the slip coefficient α depends only on the geometric characteristics of the porous surface in Stokes flow provided the width of the channel is larger than a few pore diameters (Prat and Schmitz, 1995). In the problem under consideration, the aspect ratio $h^*=h/r$ is very high. Typically, microfiltration membrane systems have support duct heights of about 1 millimeter, while the diameter of the pores

of the membrane is about equal to 1 micrometer. Thus, h^* is about 1,000. On the other hand, as α is here an intrinsic property of the surface, it is not necessary, and it would be in fact numerically impossible, to determine α for a tube or a channel of such an aspect ratio. We can in fact consider a channel of much smaller width. It turns out that a width of the order of a few pore diameter is sufficient, so we took $\delta = 5r$. As a matter of fact, we solve a problem identical to Problem 2 except for the boundary condition at $x = \delta$, which becomes $u = 0$, $(\partial v/\partial x) = 0$, $(\partial w/\partial x) = 0$. From this computation, the average velocity in the y direction at $x = \delta$ is determined,

$$\langle v \rangle_\delta = \frac{1}{b^2} \int_{-b/2}^{b/2} \int_{-b/2}^{b/2} v(\delta, y, z)\, dy dz. \tag{89}$$

This velocity can be expressed in terms of the Poiseuille velocity, v_{ph}, which is the velocity at $x = h$ that one would obtain if the channel walls were not porous, and the slip velocity v_s, that is, $\langle v \rangle_\delta = v_{ph} + v_s$. In dimensionless form we obtain

$$\langle v^* \rangle_{\delta^*} = \frac{\langle v \rangle_\delta}{v_{ph}} = 1 + \frac{2}{\alpha \delta^*}, \tag{90}$$

which leads to

$$\alpha = \frac{2}{\delta^* (\langle v^* \rangle_{\delta^*} - 1)}. \tag{91}$$

In Eq. 88 $\sqrt{K}$ is in fact a pore length scale. To obtain Eq. 90, we have taken $2r$ as pore length scale. Note also that we are dealing with an anisotropic porous medium for which the filtration velocity components in the directions parallel to the porous surface are obviously equal to zero, that is, $V = 0$ in Eq. 88. In other terms, the slip boundary condition takes here the form,

$$\left. \frac{\partial \bar{v}}{\partial x} \right|_{x=0} = -\frac{\alpha}{2r} v_s, \tag{92}$$

in which

$$\left. \frac{\partial \bar{v}}{\partial x} \right|_{x=0} = \frac{\delta}{\mu} F_y$$

(Note that in Stokes flow, a driving pressure gradient being given, the average shear stress at the porous wall is identical to the one that one would obtain if the wall was not porous, i.e., solid.) Once the slip coefficient has been determined, we can go back to Problem 1 and express the boundary condition at $x = \delta$ according to Eq. 59.

Numerical Procedure

This three-dimensional numerical approach of fluid flow in the porous wall region is performed in velocity-pressure formulation using a finite element method. This method is very appropriate in discretizing the complex periodic geometry of the system under consideration. Therefore we take prismatic elements of rectangular or triangular cross section. The velocity functions u, v, and w are chosen quadratic in x, y, and z due to the second-order partial differential in the system. The pressure function interpolation is linear. The Galerkin scheme is applied for the integration of the residue. The integrations on each element are performed using the Gauss-point integration technique. The main matrice is stored in compressed-diagonal storage mode and the final linear system is solved using a conjugate gradient squared method.

Finite elements are very convenient for imposing spatially periodic boundary conditions. The periodicity of unknown functions is imposed by numerical identification of, on the one hand, the nodes located at $y = b/2$ and $y = -b/2$, and, on the other hand, of the nodes located at $z = b/2$ and $z = -b/2$. This means that in the node numbering of the mesh, the numbers of the nodes located at $y = b/2$ are the same as the numbers of the nodes located at $y = -b/2$. Similarly, the numbers of the nodes located at $z = b/2$ are the same as the numbers of the nodes located at $z = -b/2$. Furthermore, from Eq. 35, one obtains

$$F_y^* = h^{*-2} \left(\frac{h^*}{\delta^*} \right) \left[\frac{-3 + \frac{81}{35} Re_w}{1 + \frac{Re_w}{35}} \right], \tag{93}$$

which shows that, within the framework of our assumptions (see the section on the near wall model), F_y^* is independent of y. Thus, for a given Re_w, F_y^* can be considered as a constant within the computational domain.

Because it is not easy to represent graphically a three-dimensional flow in its complete form, dividing streamlines are of special interest. These streamlines form a curve bundle, drawing a fluid-capture tube within which the fluid is sucked into the pore. They are determined from the following equation, since they are identical to the fluid particle trajectories in stationary flow:

$$\frac{dx}{dt} = \boldsymbol{u}. \tag{94}$$

The pore edge is discretized into 100 points, each point being the final point of a dividing streamline. Therefore the set of Eq. 94 is integrated numerically 100 times from any of these points to the far upstream point located at the upstream boundary of the domain, that is, the $y = -b^*/2$ plane. We use a fourth-order Runge–Kutta technique with a time step based on half times the smallest width of the smallest element divided by the highest local velocity component to obtain a good accuracy. Furthermore, in practice, the numerical integration procedure begins at an initial point located at a negligible distance from the pore edge, $x = 0$ and $y^2 + z^2 = 1 - 0.01$ to avoid the singularity in the flow field at exact edge. Yan et al. (1991) have confirmed that this approximation produces no significant errors in the capture tube shape.

Results and Discussion

The first step of the analysis of the flow in the vicinity of a porous surface with suction consists of determining the un-

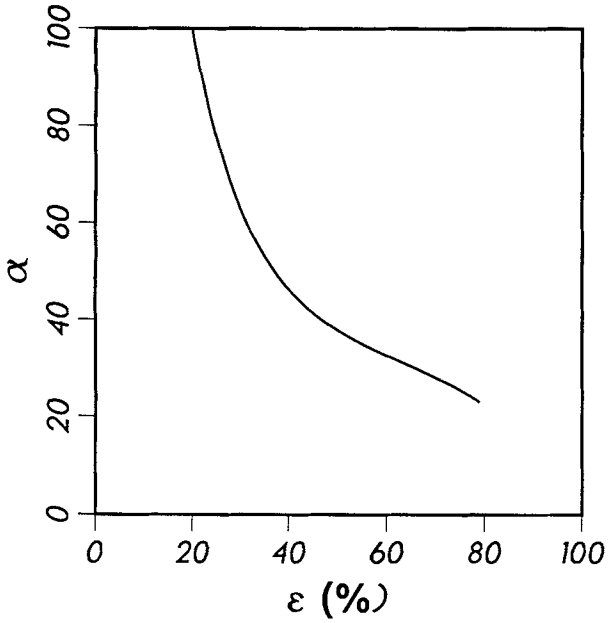

Figure 3. Variation of the slip coefficient α as a function of the surface porosity ϵ.

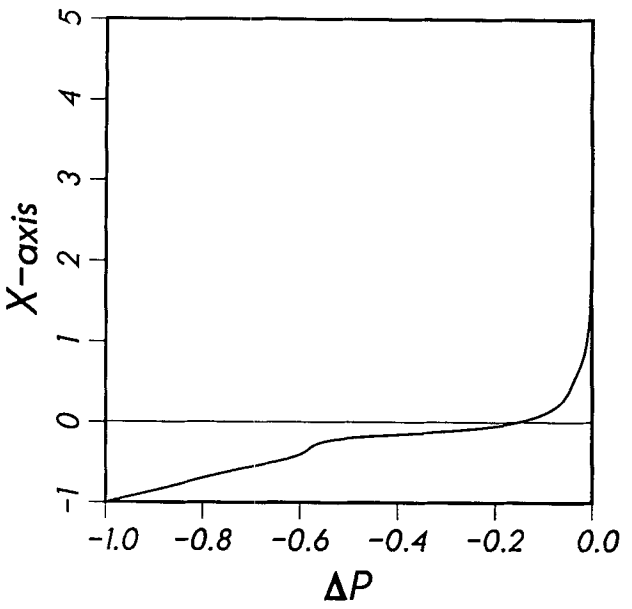

Figure 4. Transverse variation of mean pressure in the $z = 0$ plane for Problem 2.

known slip coefficient α. As discussed in the section on the slip coefficient, determining this parameter is necessary to solve the local problem formulated in the section on the superposition principle.

Study of the slip effect

The slip coefficient α is determined, as described earlier, for various surface porosities. Results are plotted in Figure 3. The slip effect is naturally greater in the case of high porosity than in the case of low porosity. Note that the greater the slip effect, the smaller the slip coefficient α. Now we go back to the local problem, Eqs. 23–32, and compare the magnitude of the slip velocity to the corresponding Poiseuille velocity at $x = \delta$. As can be seen from Table 1, v_s can be ignored in Eq. 25. In fact, from a practical standpoint, the slip effect is almost always negligible as far as microfiltration is concerned because of the high aspect ratio of the hollow fibers (see the section on the superposition principle). This result was previously suggested by Belfort and Nagata (1985) for all the pressure-driven membrane processes from estimations of slip-velocity coefficients for typical operating conditions. In addition, as pointed out by Saffman (1971), the slip coefficient α is intimately associated with the precise location of the porous wall–plain fluid region interface. Due to the uncertainty of this location in practice, the slip effect is not only generally weak but also extremely difficult to model. Naturally, under certain very particular circumstances, however, taking the slip effect into account is essential (see for instance, Prat et al., 1994).

Table 1. Ratio of the Slip Velocity to the Poiseuille Velocity at $x = \delta$ as a Function of the Porosity

ϵ %	20	35	55	79
$v_s/v_{p\delta}$	0.004	0.008	0.011	0.017

Pressure drop across the pore

Regarding the flow in the x direction, it is of interest to study the pressure drop between the plane $x = \delta$, that is, the upper boundary of the computational domain, and the pore exit. Note that there is no pressure drop across the pore due to the flows associated with Problems 1 and 2. The pressure drop is only due to the flow represented by Problem 3. As can be seen from Figure 4, which shows a typical mean pressure distribution associated with Problem 2 in the $z = 0$ plane, the pressure drop essentially occurs in the vicinity of the pore opening and across the pore. In their study on the creeping motion through an orifice, Dagan et al. (1982) have shown that the relation between the pressure drop ΔP across the pore and the volumetric flow rate Q through the pore can be expressed as

$$\Delta P = \left(\frac{8d}{r\pi} + 3\right)\frac{Q\mu}{r^3}. \tag{95}$$

Note that here ΔP, Q, d, r are dimensional variables. The first term in the r.h.s. of Eq. 95 is the pressure drop across the pore due to the Poiseuille flow through the pore. The second term accounts for the pressure drop in the vicinity of the pore opening. This term is equal to the pressure drop experienced by a fluid flowing through a circular hole in a plane, Sampson (1891). Thus, as far as the pressure drop is concerned, the flow can be envisioned as a linear combination of a Poiseuille flow and a Sampson flow. Contrary to the case studied by Dagan et al. (1982), a Poiseuille profile is imposed at the pore exit in the present study. Therefore, the pressure drop associated with the Sampson flow is not taken into account at the pore exit in our case. Since we are dealing

Table 2. Computed Values of the Pressure Drop Coefficient across the Pore as a Function of the Porosity

ϵ %	20	35	55	79
Π_c	4.105	4.090	3.960	3.700

with creeping flows, the pressure drop across the pore can be deduced from Eq. 95 by taking into account half the Sampson flow contribution, since our pore has one entrance but in fact no exit,

$$\Delta P = \Pi(d/r)\frac{Q\mu}{r^3}, \tag{96}$$

where

$$\Pi(d/r) = \left(\frac{8d}{r\pi}\right) + 1.5. \tag{97}$$

In dimensionless form, it leads to Eqs. 98 and 99,

$$\Delta P^* = \frac{r\Delta P}{\mu u_\delta} = \Pi(d^*)b^{*2}, \tag{98}$$

$$\text{where } \Pi(d^*) = \frac{8}{\pi}d^* + 1.5. \tag{99}$$

In our study, the aspect ratio $d^* = d/r$ is kept constant, $d/r = 1$. As can be seen from Table 2, in which computed values of $\Pi(d^*)$, denoted by Π_c in Table 2, are reported for the various cases considered in the present study, our results are in close agreement with Eq. 97, giving $\Pi(d^*) = 4.046$. We note a weak decrease of Π_c as ϵ increases. This can be attributed to the neighbor pore blocking effect that is discussed in the next section. This effect limits the lateral expansion of the flow and increases with the porosity. This leads to differences in the flow structure between the Sampson flow case and the one considered in the present study. Therefore, the discrepancy between the pressure drop given by the Sampson flow solution and the one numerically computed in the pore entrance region may reasonably be expected to increase with the porosity, in agreement with the data in Table 2.

Fluid flow near a pore with suction

As this study concerns Stokes flow, all the simulations are only performed for a single macroscopic mean pressure gradient F_y^*, chosen arbitrarily to correspond to a Reynolds number equal to 100 in the channel at the location of the considered cell of the membrane. Therefore the local Reynolds number $Re_\delta = (\bar{v}_\delta \delta/\nu)$ is also kept constant throughout the study. As explained before, the local Reynolds number is much smaller than 1 because of the high aspect ratio h^*, taken here equal to 500. These operating conditions correspond to a hollow fiber cross-flow microfiltration process. As mentioned previously, a height δ^* equal to 5 is sufficient to verify the assumption of uniform velocity at the upper fluid surface of the domain. The depth of the pore d^* is taken equal to 1, that is, one pore radius, allowing us to assume a fully developed flow at the bottom of the pore as boundary condition, Eq. 26. Dagan et al. (1982) have indeed demonstrated that the pore axial velocity approaches a Poiseuille profile with less than 1.5% deviation after a short entrance distance equal to half the pore radius. In the limit of very small Re_w, however, the boundary condition at the exit of the pore becomes questionable since in this case the imposed boundary condition amounts to imposing a no-slip boundary condition at the exit of the pore, that is, it amounts to assuming a solid wall closing the pore. As demonstrated, for instance by Higdon (1985) in two-dimensions, the structure of the flow within the pore depends on the pore aspect ratio, that is, here, d^*. Thus, some errors are certainly introduced by this boundary condition at very low Re_w. However, the main qualitative aspects, such as the occurrence of recirculating eddies, are probably not affected. Furthermore, in what follows, we focus on cases for which the flow within the pore is dominated by the solution of Problem 3, that is, cases for which the suction is sufficient to ensure a Poiseuille profile at the exit of the pore.

Computations were performed for various surface porosities ϵ, ranging from 20% to 80% and in a large range of suction conditions, Re_w varying from 0. to 1. We study the three-dimensional flow over the porous surface by computing the associated fluid capture tube within which the fluid is sucked into the pore. We also focus on the velocity field inside the pore.

Influence of Suction Intensity. Figure 5a to 5c shows the fluid capture tubes corresponding to $\epsilon = 20\%$ for $Re_w = 0.01$, 0.1, and 1. Not surprisingly, we observe that the three-dimensional effect, that is, the fact that the z velocity component w is not equal to zero, is more significant when we increase the suction intensity. This effect is quasi nonexistent at low Re_w since each dividing streamline stays in a constant z plane. The resulting fluid capture tube is nearly a two-dimensional elliptical cylinder whose width is roughly equal to the pore diameter and whose height diminishes from the $y = -b/2$ upstream plane and becomes flat at the downstream edge of the pore where it tends to 0 (Figure 5a). On the contrary, for the larger values of Re_w, the width of the fluid capture tube cross section at $y = 0$ extends far beyond the boundary of the pore, characterizing a three-dimensional flow feeding the pore. Moreover for the highest values of Re_w, the tube cross section also extends downstream from the pore, that is, some fluid trajectories turn back toward the downstream sharp corner of the pore (Figure 5c). Streamwise sections of the fluid capture tube in the $z = 0$ symmetry plane are shown in Figure 6. Cross sections of the fluid capture tube in the $y = -b/2$ upstream plane are depicted in Figure 7. The existence of these two phenomena, lateral expansion and downstream turning back of the suction flow, is confirmed by Figure 8, in which the velocity field at the mouth of the pore is shown for a wide range of Re_w. One observes that each z-velocity component rapidly diminishes as Re_w becomes lower, and can even be neglected when Re_w is smaller than 0.01, which indicates a quasi two-dimensional flow over the porous surface. Let us now turn our attention to the analysis of the flow through the pore in order to confirm the existence in some cases of a recirculating vortex inside the pore, depending on the suction intensity, already revealed by previous works (Tutty, 1988; Schmitz et al., 1992).

In Figure 9a to 9d, which presents some velocity fields in

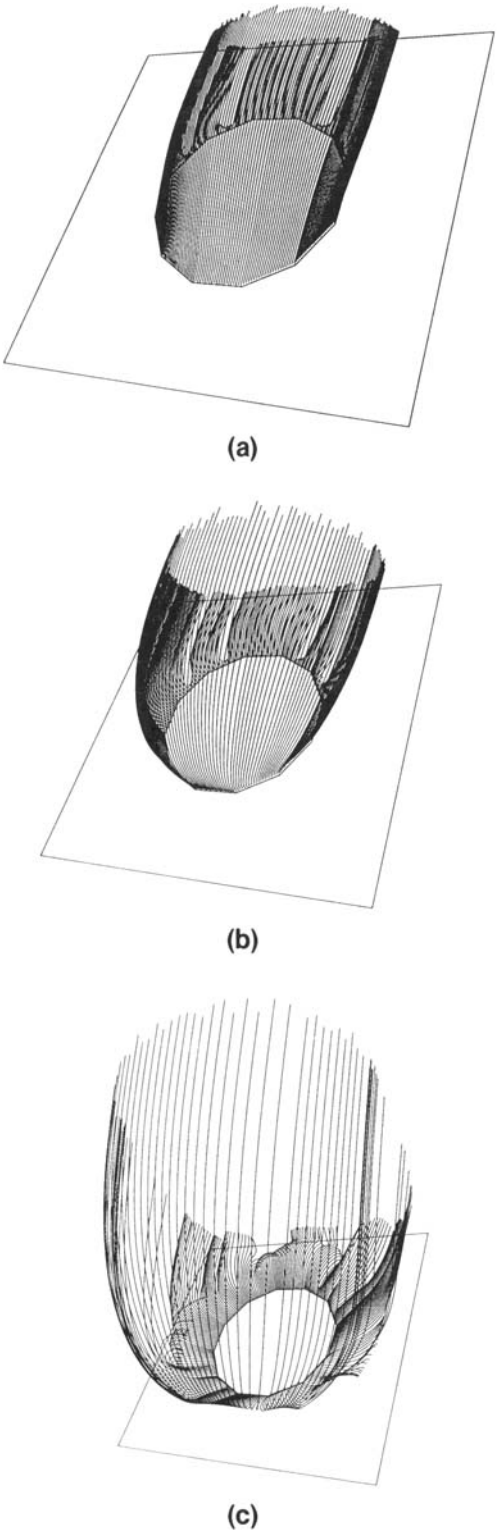

Figure 5. Variation of the fluid capture tube with the suction intensity for $\epsilon = 20\%$.

(a) $Re_w = 0.01$; (b) $Re_w = 0.1$; (c) $Re_w = 1$.

the $z = 0$ symmetric plane, we clearly visualize the birth and the growth of a clockwise-rotating vortex when Re_w is reduced. The vortex appears at the upstream edge of the pore when Re_w is on the order of 0.01, that is, when Re_w is very low. Let us note that this value is consistent with the one that had been determined in the two-dimensional approach (Schmitz et al., 1992). When Re_w decreases, the vortex grows and moves. One observes the displacement of its center from the upstream upper corner to the middle of the pore when the suction magnitude decreases. The limit case of no suction flow is associated with an eddy perfectly centered in the middle of the pore occupying almost all the pore volume. Therefore when the suction exists and the vortex is present, advection through the pore occurs only near the downstream edge of the pore, as shown in Figure 9a. On the contrary, when Re_w is higher, the eddy vanishes. In this case the fluid that is sucked up fills all of the pore volume (Figure 9d). Furthermore, the volume of the fluid capture tube increases since the suction magnitude becomes more important. The different flow structures obtained can, therefore, be classified into two categories depending on the existence of this eddy inside the pore, that is, according to whether Re_w is less or greater than about 0.01. As far as microfiltration is concerned, this shows that there is no eddy inside the pore under usual circumstances since the eddies are only observed for very small Re_w.

Influence of Surface Porosity. Despite the fact that porous surfaces such as nucleopore membranes are generally of small porosity, other porous materials may be of high surface porosity. In particular, the surface of a deposit of particles aggregated over the membrane during a cross-flow microfiltration process can be schematically considered as a flat porous surface of high porosity and of spatially periodic geometry similar to our model porous surface. So it is of interest to study the effect of the surface porosity, ϵ, on the shape of the fluid capture tube. Figures 10a to 10c show the fluid capture tubes corresponding to $Re_w = 0.2$ for $\epsilon = 20\%$, 35%, and 80%. As can be seen from Figures 11 and 12, the height and the width of the fluid capture tube decreases with ϵ. Not surprisingly the feeding of the pore by downstream turning back is also reduced as ϵ increases, as shown in Figure 11. In

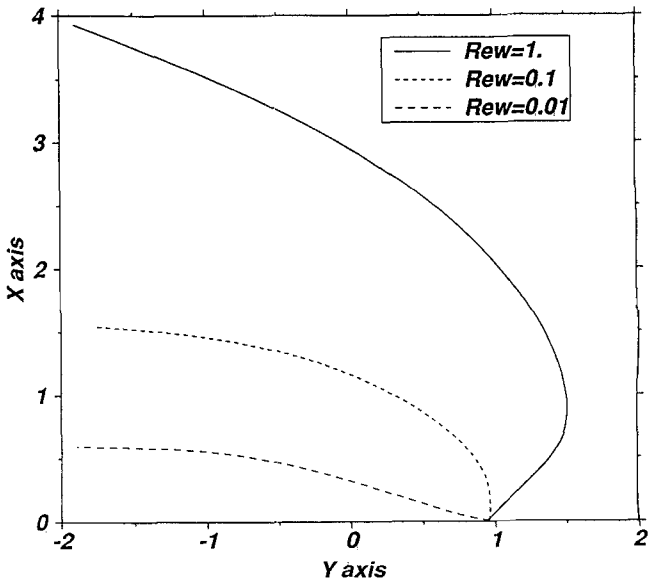

Figure 6. Streamwise sections of the fluid capture tube in the $z = 0$ plane for $\epsilon = 20\%$.

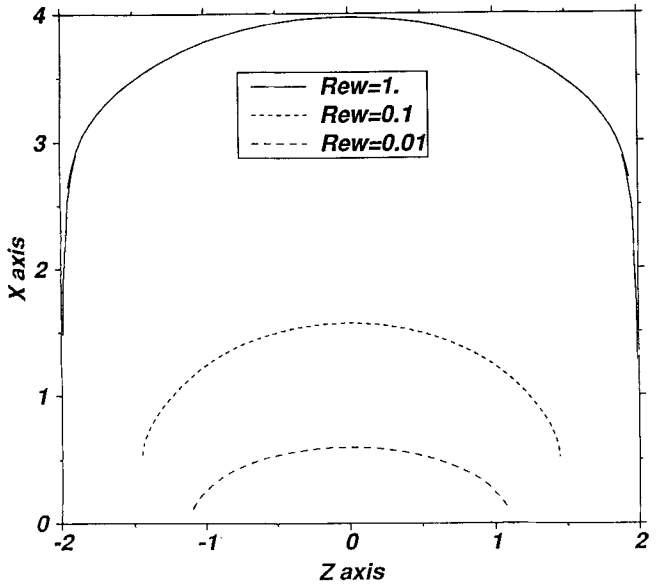

Figure 7. Cross sections of the fluid capture tube in the $y = -b/2$ plane for $\epsilon = 20\%$.

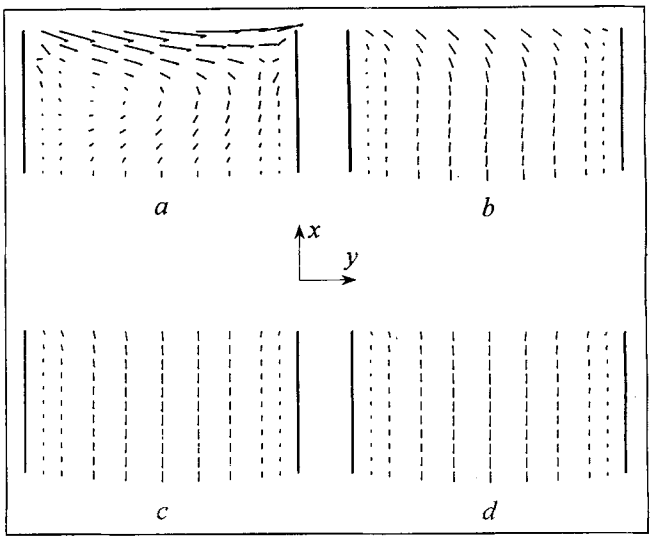

Figure 9. Velocity fields inside the pore in the $z = 0$ plane for $\epsilon = 20\%$.

(a) $Re_w = 0.001$; (b) $Re_w = 0.01$; (c) $Re_w = 0.1$; (d) $Re_w = 1$.

another respect, we clearly see in Figure 10c the saturation of lateral expansion of the fluid capture tube as ϵ becomes higher. This is clearly evidenced by Figure 13, which shows the evolution of the capture tube extent in the z direction in the $y = -b/2$ plane as a function of ϵ and Re_w. Case ϵ, equal to 80%, appears as the limit case that corresponds to a quasi square cross section at $y = -b/2$, suggesting a quasi-two-dimensional case. Before the lateral saturation is reached, the lateral expansion of the capture increases as ϵ decreases and Re_w increases, as can be seen from Figure 13. As discussed earlier, results reveal a higher fluid region over the porous surface concerned by suction, as ϵ is smaller and Re_w is greater. This is summarized in Figure 14, which shows the evolution of the capture tube extent in the x direction in the $y = -b/2$ plane as a function of ϵ and Re_w.

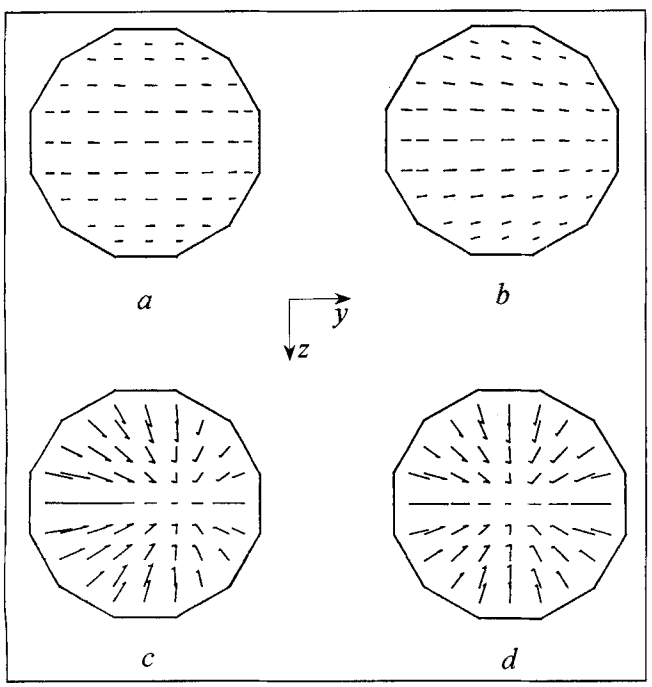

Figure 8. Velocity fields at the mouth of the pore ($x = 0$ plane) for $\epsilon = 20\%$.

The fluid flows from right to left. (a) $Re_w = 0.001$; (b) $Re_w = 0.01$; (c) $Re_w = 0.1$; (d) $Re_w = 1$.

Feeding of Successive Pores. Particle aggregation, not only at the porous surface but also inside the pores, depends drastically on the flow in the vicinity of the porous surface and more precisely on the fluid flow toward the numerous collecting pores of the porous surface. Therefore it is interesting to characterize the fluid capture tubes of several successive pores. We have drawn in Figures 15a to 15c the fluid capture tubes related to three pores in series on a porous surface having a porosity of 20% for $Re_w = 0.1$. The first pore is located in the middle of the cell shown in Figure 15, the second and third pores being located downstream of this cell. As can be seen from Figure 15, the upper boundary of the first pore capture tube, Figure 15a, forms the lower boundary of the second pore capture tube, Figure 15b. The upper boundary of the second pore capture tube, in turn, forms the lower boundary of the third pore capture tube, Figure 15c. The part of the third pore fluid capture tube located above the considered cell, that is, the first pore cell, appears to be almost not modified by the suction into the first and the second pores, the streamlines being quasi straight within this part of the third pore capture tube. This is well-confirmed in Figure 16, in which streamwise sections of the capture tubes are represented in the $z = 0$ plane. One observes that the thickness of the capture tubes above the first pore cell becomes uniform for the capture tubes associated with the furthest downstream pores. However, the flow is not parallel within the capture tubes, as can be seen from Figure 17, which reveals the right and left expansion of the cross sections of the capture tubes in the $y = -b/2$ plane. Note that the curve associated with the fourth pore in Figure 17 is also the curve asso-

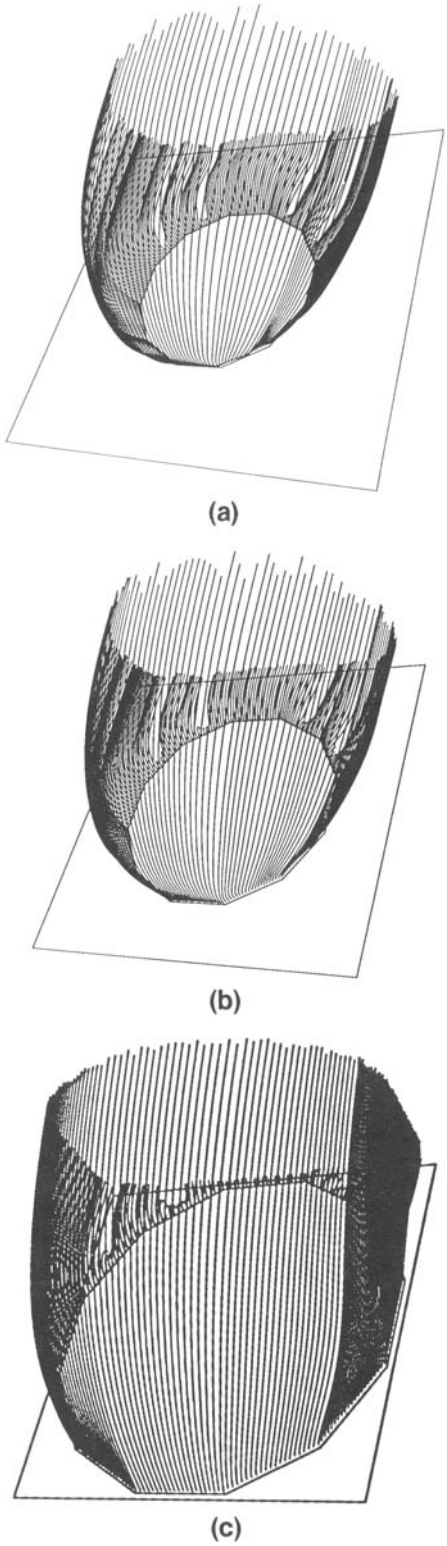

Figure 10. Variation of the fluid capture tubes with the surface porosity for $Re_w = 0.2$.

(a) $\epsilon = 20\%$; (b) $\epsilon = 35\%$; (c) $\epsilon = 80\%$.

ciated with the fifth pore in the plane $y = b/2$ because of the spatial periodicity. Figure 17 makes clear that the lateral expansion of the capture tube of a given pore diminishes from far upstream up to the pore. For a porous surface of higher

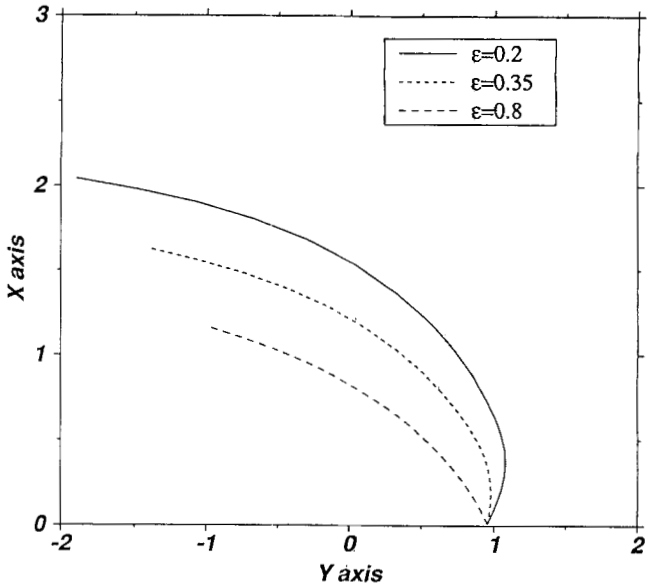

Figure 11. Streamwise sections of the fluid capture tube in the $z = 0$ plane for $Re_w = 0.2$.

porosity, the phenomenon of neighbor pore blocking is clearly evidenced in Figure 18, in which are plotted upstream cross sections of fluid capture tubes corresponding to fluid suction through successive pores. Indeed in this typical case, for the same suction condition as in Figure 17, we observe a quasi vertical expansion of the fluid capture tubes. This is due to the influence of neighbor pores as discussed below.

Influence of Neighbor Pores. As can be seen from Figure 7, Figure 13, or Figure 18, the lateral expansion of the fluid capture tube cannot exceed the limits of the spatial period in the z direction. Clearly, the presence of lateral neighbor pores reduces the possibility given to the fluid to pass to left and right of the pore. In other words, the influence of neighbor

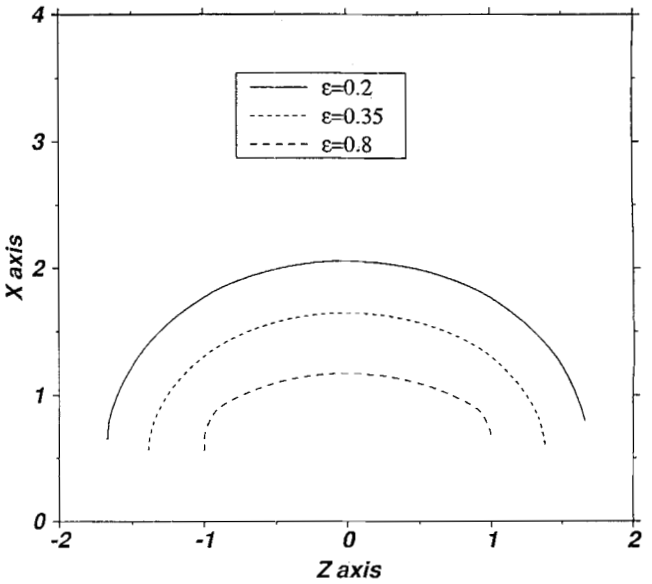

Figure 12. Cross sections of the fluid capture tube in the $y = -b/2$ plane for $Re_w = 0.2$.

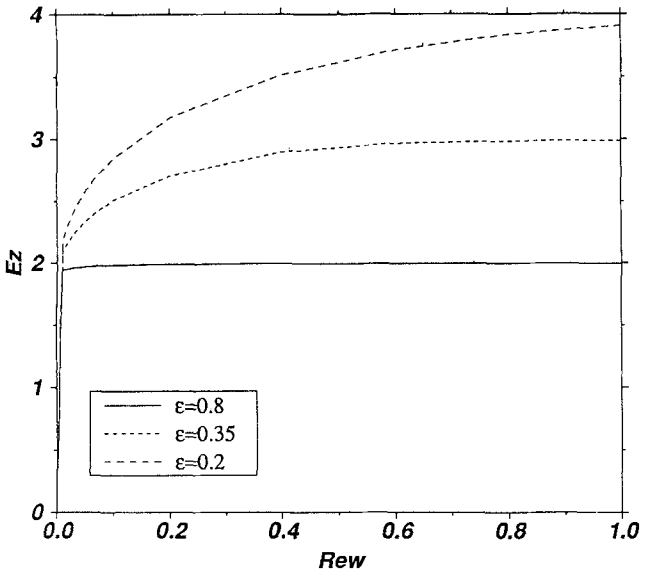

Figure 13. Capture tube horizontal extent in the $y = -b/2$ plane as a function of ϵ and Re_w.

pores here prevents the lateral expansion of the fluid capture tube. This is the most striking feature of the fluid capture tubes at high suction rate when our results are compared with those of Tutty (1988) and Yan et al. (1991), who have studied the fluid capture tube of an isolated pore. In this latter case, the lateral expansion of the fluid capture tube at relatively high suction height is significantly greater. Naturally, as the lateral expansion is not limited in this case, the height of the fluid capture tube is significantly lower than the one observed in our simulations. This effect, which is due to the influence of neighbor pores, is termed the neighbor pore-blocking effect. Thus, in the case of the spatially periodic membrane, part of the fluid that is sucked into the pore comes from regions of relatively larger tangential velocities.

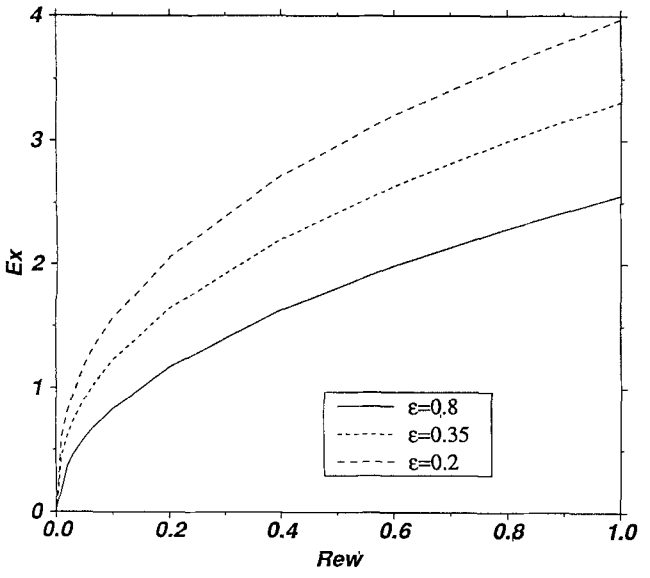

Figure 14. Capture tube vertical extent in the $y = -b/2$ plane as a function of ϵ and Re_w.

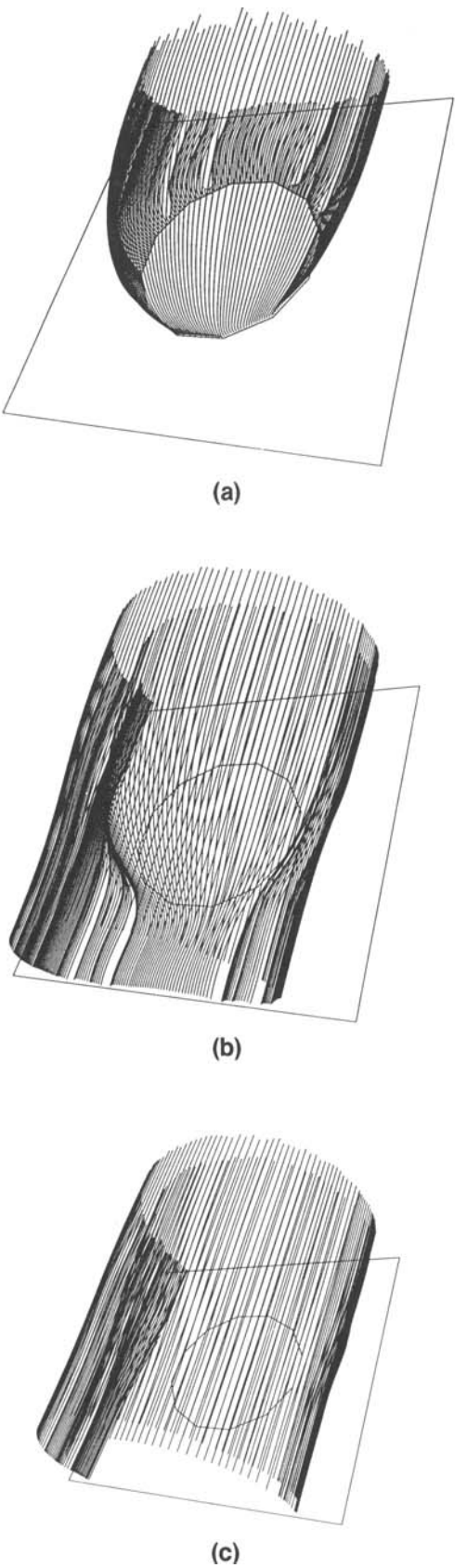

Figure 15. Fluid capture tubes of successive pores for $\epsilon = 20\%$ and $Re_w = 0.1$.

(a) pore of the considered cell; (b) first pore downstream; (c) second pore downstream.

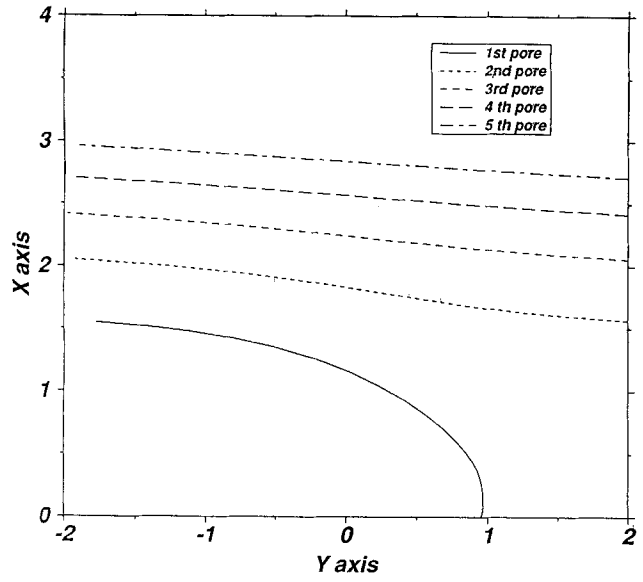

Figure 16. Streamwise sections of the fluid capture tube of successive pores in the $z=0$ plane for $\epsilon = 20\%$ and $Re_w = 0.1$.

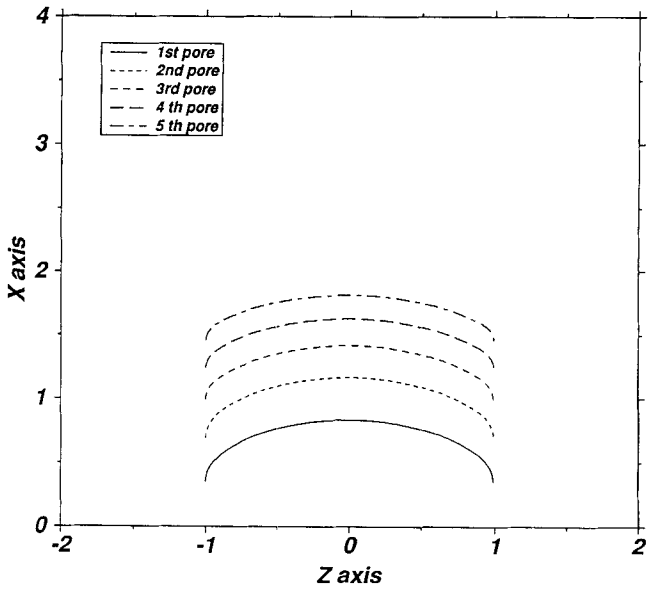

Figure 18. Cross sections of the fluid capture tubes of successive pores in the $y=-b/2$ plane for $\epsilon = 80\%$ and $Re_w = 0.1$.

Conclusions

In this article, a finite element solution to the three-dimensional laminar stationary flow over a porous surface with suction has been presented. This work accounts for interacting pores by the use of periodic boundary conditions. Since the flow in the vicinity of the porous wall can be approximated by a Stokes flow, the complex three-dimensional flow has been treated as a superposition of three simpler flows, a shear flow parallel to the porous wall, a pressure-driven flow parallel to the porous wall, and a pressure-driven flow normal to the porous wall. Several aspects of the flow have been analyzed.

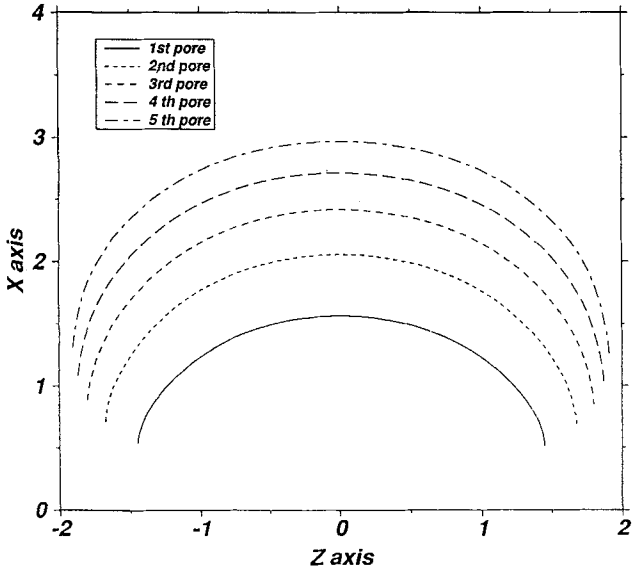

Figure 17. Cross sections of the fluid capture tube of successive pores in the $y=-b/2$ plane for $\epsilon = 20\%$ and $Re_w = 0.1$.

The study of the low suction intensity case shows the existence of a recirculating eddy that grows from the upstream edge of the pore as suction intensity decreases. The slip effect associated with the flow over a porous surface is here negligible even for a surface porosity as high as 80%. In the authors' opinion, the slip effect can be neglected in most of the cross-flow microfiltration systems. The pressure drop in the direction normal to the porous wall is due to the deformation of the streamlines in the vicinity of the pore opening and to the flow through the pore. In agreement with the results of Dagan et al. (1982), this pressure drop can be simply determined by assuming Poiseuille flow throughout the pore and Sampson's solution outside, Eq. 96. Most of our other results concern the fluid capture tube under various suction magnitudes and surface porosities. At high suction rates, particular phenomena such as the capture tube lateral expansion, which exemplifies the three-dimensional structure of the flow and the downstream turning back of the suction flow in the vicinity of the pore entrance have been seen. At a low suction rate, the fluid capture tube is flat and its width is about that of the pore diameter. Although our results are in qualitative agreement with the results of Tutty (1988) and Yan et al. (1991) concerning the flow over and into an isolated pore, we observe significant differences due to the fact that the influence of neighbor pores is taken into account in our simulations. Compared to the results of Tutty (1988) and Yan et al. (1991), the influence of neighbor pores essentially results in limiting the lateral expansion of the capture tube at high suction rates and in increasing its vertical expansion, the so-called neighbor pore blocking effect. Thus, at high suction rates, the fluid sucked into a pore comes from regions of relatively greater tangential velocities. Because of this limited lateral expansion phenomenon, the flow within the capture tube is almost two-dimensional in the limit of high porosities and suction rates. The study of the capture tubes associated with a sequence of pores shows that the fluid feeding a given

pore comes from regions located upstream, so that the further upstream the region is located, the greater the average tangential velocity. Naturally, we have considered one single type of pore arrangement at the surface, namely a square lattice. It would certainly be interesting to study other arrangements, such as a hexagonal lattice. However, we do not believe that this would significantly modify our results.

Acknowledgments

The authors wish to thank the Centre de Compétence en Calcul Numérique Intensif and the Centre National Universitaire Sud de Calcul de Montpellier for computing support. We also would like to acknowledge the very constructive input of the reviewers of the paper.

Notation

E_x = capture tube vertical extent in the $y = -b/2$ plane
E_z = capture tube horizontal extent in the $y = -b/2$ plane
Re = channel Reynolds number $= (2v_D h/\nu)$
$\mathbf{u}^*$ = dimensionless velocity vector
u_δ = x-axis velocity component at $x = \delta$
u_w = mean wall suction velocity
$\bar{v}_\delta$ = velocity at $x = \delta$
$v_{p\delta}$ = Poiseuille velocity at $x = \delta$
x = x-axis coordinate
$\mathbf{x}$ = coordinate vector
y = y-axis coordinate
z = z-axis coordinate

Greek letters

δ = near wall region thickness
γ_v = velocity ratio $= u_p/\bar{v}_\delta$
Γ_f = area of the fluid phase at the porous wall
Γ_s = area of the solid phase at the porous wall
λ = scale ratio $= r/h$
μ = fluid dynamic viscosity
ρ = fluid density

Literature Cited

Beavers, G., and D. Joseph, "Boundary Conditions at a Naturally Permeable Wall," *J. Fluid Mech.*, **30**, 197 (1967).
Belfort, G., and N. Nagata, "Fluid Mechanics and Cross-Flow Filtration: Some Thoughts," *Desalination*, **53**, 57 (1985).
Berman, A. S., "Laminar Flow in Channels with Porous Walls," *J. Appl. Phys.*, **24**, 1232 (1953).
Brady, J. F., "Flow Development in a Porous Channel and Tube," *Phys. Fluids*, **27**(5), 1061 (1984).
Dagan, Z., S. Weinbaum, and R. Pfeffer, "An Infinite-Series Solution for the Creeping Motion Through an Orifice of Finite Length," *J. Fluid Mech.*, **115**, 505 (1982).
Durlofsky, L., and J. F. Brady, "The Spatial Stability of a Class of Similarity Solutions," *Phys. Fluids.*, **27**(5), 1068 (1984).
Higdon, J. J. L., "Stokes Flow in Arbitrary Two-Dimensional Domains: Shear Flow Over Ridges and Cavities," *J. Fluid Mech.*, **159** 195 (1985).
Kaviany, M., *Principles of Heat Transfer in Porous Media*, Mechanical Engineering Series, Springer-Verlag, New York/Berlin (1991).
Larson, R. E., and J. J. L. Higdon, "Microscopic Flow near the Surface of Two-Dimensional Porous Media: I. Axial Flow," *J. Fluid Mech.*, **166**, 449 (1986).
Larson, R. E., and J. J. L. Higdon, "Microscopic Flow near the Surface of Two-Dimensional Porous Media: II. Transverse Flow," *J. Fluid Mech.*, **178**, 119 (1987).
Prat, M., and P. Schmitz, "Boundary Conditions for Laminar Flows in Rough and Porous Channels," in preparation (1995).
Prat, M., P. Schmitz, and D. Poulikakos, "On the Effect of Surface Roughness on the Vapor Flow under Leidenfrost-Levitated Droplets," *ASME J. Fluid Eng.*, in press (1995).
Saffman, P. G., "On the Boundary Condition at the Surface of a Porous Medium," *Stud. Appl. Math.*, **50**, 93 (1971).
Sampson, R. A., "On Stokes' Current Function," *Phil. Trans. R. Soc. London Ser.*, **A182**, 449 (1891).
Schmitz, P., D. Houi, and B. Wandelt, "Hydrodynamic Aspects of Crossflow Microfiltration. Analysis of Particle Deposition at the Membrane Surface," *J. Membrane Sci.*, **71**, 29 (1992).
Singh, R., and R. L. Laurence, "Influence of Slip Velocity at a Membrane Surface on Ultrafiltration Performance II—Tube Flow System," *Int. J. Heat Mass Transfer*, **12**, 731 (1979).
Tanahashi, T., H. Kawai, J. Masuzawa, T. Sawada, and T. Ando, "Flow of the Entrance Region in a Porous Pipe (3rd Report: Transient Flow)," *Bull. JSME*, **25**, 1070 (1982).
Terril, R. M., "Laminar Flow in a Uniformly Porous Channel," *Aeronautics*, **15**, 297 (1964).
Terril, R. M., and P. W. Thomas, "On Laminar Flow Through a Uniformly Porous Pipe," *Appl. Sci. Res.*, **21**, 37 (1969).
Tutty, O. R., "Flow in a Tube with a Small Side Branch," *J. Fluid Mech.*, **191**, 79 (1988).
Vignes-Adler, M., P. M. Adler, and P. Gougat, "Transport Processes Along Fractals. The Cantor-Taylor Brush," *Phys. Chem. Hydrodyn.*, **8**, 401 (1987).
Wu, W. Y., S. Weinbaum, and A. Acrivos, "Shear Flow over a Wall with Suction and Its Application to Particle Screening," *J. Fluid Mech.*, **243**, 489 (1992).
Yan, Z. Y., A. Acrivos, and S. Weinbaum, "Fluid Skimming and Particle Entrainment into a Small Circular Side Pore," *J. Fluid Mech.*, **229**, 1 (1991).

Manuscript received Feb. 18, 1994, and revision received Nov. 8, 1994.